Fucosylated oligosaccharide Lacto-*N*-fucopentaose I ameliorates enterovirus 71 infection by inhibiting apoptosis

Xiaoxiang Gao [a,1], Yinghui Qiu [a,1], Luying Gao [b], Lizhu Zhang [a], Xiaoqing Li [a], Yuanyuan Liu [a], Chao Zhao [a,c,*]

[a] *College of Food Science, Fujian Agriculture and Forestry University, Fuzhou 350002, China*
[b] *Department of Pediatrics, Nanjing First Hospital, Nanjing Medical University, Nanjing, 210006, China*
[c] *Key Laboratory of Marine Biotechnology of Fujian Province, Institute of Oceanology, Fujian Agriculture and Forestry University, Fuzhou 350002, China*

ARTICLE INFO

ABSTRACT

Enterovirus 71 (EV71) is the main cause of hand, foot and mouth disease that results in high rates of severe diseases in small children. Lacto-*N*-fucopentaose I (LNFPI) can inhibit pathogen invasion and regulate intestinal flora. However, whether LNFPI inhibits EV71 infection remains unknown. In this study, we examined the effect and mechanism of LNFPI against EV71. LNFPI reduced capsid protein VP1 to block virus adsorption, inhibited cyclin E transcription and promoted CDK2 expression in EV71-induced human rhabdomyosarcoma cells, thereby causing virus-induced S phase arrest and inhibiting death receptor and mitochondria-induced apoptosis. The effects of LNFPI on apoptosis were further confirmed in *Caenorhabditis elegans*. The correlation analysis revealed that LNFPI inhibited cell apoptosis by reducing the abundance of *Sphingomonas*, *Stenotrophomonas* and *Achromatic*, which are associated with pro-apoptotic genes in *C. elegans*, and by increasing the abundance of *Micromonospora*, which is related to apoptotic inhibition. These findings lead to further recommendations for LNFPI supplementation in infant formula, as it could offer antiviral benefits to formula-fed infants.

1. Introduction

Human milk oligosaccharides (HMOs) are the third most nutritious ingredient in human milk, which have evoked great interest because of their beneficial effects on infants' health and intestinal bacteria and the inhibition of pathogens (Lars and Evelyn, 2012; Plaza-Díaz et al., 2018). In addition, breast-fed babies are less susceptible to diseases and HMOs can be synthesised *in vitro*. Therefore, the study of HMOs has become a hot topic and has aroused increased attention among researchers (Lars and Evelyn, 2012). There are 200 types of HMOs based on their structure, which possess various biological functions according to the composition of monosaccharides (Bode and Jantscher, 2012). Lacto-*N*-fucopentaose I (LNFPI) is an HMO that can prevent viral and bacterial invasion because its structure is similar to the recognition site on the cell surface (Morozov et al., 2018). Recent studies have reported that LNFPI binds to the capsid protein through which norovirus attacks cells (Koromyslova et al., 2017). Thus, rotavirus-induced gastroenteritis in children could be deterred by binding with LNFPI (Li et al., 2014).

Enterovirus 71 (EV71) is the main etiological pathogen of the hand, foot and mouth disease, characterised by red blots on the hand, foot and mouth in babies. It also causes serious diseases such as encephalitis and polio-like paralytic disease transmitted by the faecal–oral route, transplacental route and respiratory droplets (Wang et al., 2016). The mechanism of EV71 infection has been widely investigated and involved multiple biological processes. First, EV71 infection induces oxidative stress and increases the levels of reactive oxygen species (ROS) (Tung et al., 2011). Second, EV71 infection is usually accompanied by inflammatory cell infiltration, abnormal levels of pro-inflammatory cytokines and chemokines, increased levels of interleukin IL-1β and IL-18 and oedema. Increasing IL levels could be also observed in patients with EV71 infection (Wang et al., 2017). Third, the 3C of EV71 mRNA also activates caspase-3, thereby affecting virus reproduction, and the cells transfected with 3C showed high caspase-3 levels and apoptosis rates (Li et al., 2016). Outbreaks of EV71 have occurred in Malaysia, Taiwan, Singapore and other countries causing huge property losses and have caused great concerns from Chinese health authorities (Hu et al., 2018).

The uncontrolled spread of EV71 infection may hinder a country's development because of sequelae. Although two types of vaccines have been licensed, they cannot supply and be tolerable by all people (Hu et al., 2018). Thus far, ribavirin has been widely used and easily accessible and has decreased the incidence and mortality rates of EV71 infection. However, this drug has some side effects such as anaemia, decreased haemoglobin level and cardiopulmonary disorders (Zhang et al., 2012). Thanks to ribavirin inhibiting virus invasion by resisting apoptosis, it is high time to explore and complement similar antiviral supplements that have anti-apoptotic effects, such as food supplementation that can prevent a potential pandemic (Lin et al., 2018).

Caenorhabditis elegans (*C. elegans*) has great biological significance for the discovery of cell apoptosis (Salem et al., 2018). The germ cell apoptosis of *C. elegans* occurs without any stress (Vince et al., 2011). Moreover, genes in *C. elegans* are highly homologous to those in humans. *Egl-1* and *Ced-9* located in the cytoplasm and mitochondria are homologous to Bcl-2, whereas *Ced-4* and *Ced-3* share sequence homology with Apaf-1 and caspase-3, respectively (Fan et al., 2011; Salem et al., 2018; Vince et al., 2011). Thus, it is necessary to examine gene regulation through *C. elegans*.

The gut microbiota plays an important role in providing nutrition and regulating immunity, provoking great enthusiasm. However, the microbiota could affect biological processes and homeostasis. A study reported that the gut microbiota could produce compounds or affect pathways that influence apoptosis (Feng et al., 2018). Therefore, it is essential to explore the potential relationship between gut microbiota and apoptosis. The main goal of this study was to establish a model of EV71-infected cells to investigate the roles of LNFPI synthesised using a one-pot enzymatic method on apoptosis after EV71 invasion. In addition, *C. elegans* was used to further determine the anti-apoptotic effects and intestinal flora regulation of LNFPI.

2. Materials and methods

2.1. Viruses, cells and culture medium

Human rhabdomyosarcoma (RD) cells were purchased from the Chinese Academy of Sciences (Shanghai, China) and cultured in Dulbecco's modified eagle medium (DMEM; Gibco/Invitrogen, Carlsbad, CA, USA) with 10% foetal bovine serum (HyClone, Logan, UT, USA) and 1% streptococcus penicillin solution (Beyotime Biotech, Shanghai, China) at 37 °C and 5% CO_2. The EV71 Fuyang0805 strain was obtained from Nanjing First Hospital, Nanjing Medical University. EV71 with a multiplicity of infection (MOI) of 0.5 was reproduced and propagated on RD cells cultured in DMEM with 2% FBS, and the median tissue culture infectious dose (TCID50) was measured in micro-titration analysis to determine virus titre. Briefly, RD cells (10^5 cells/well) were transplanted in 96-well plates. EV71 with gradient concentration was diluted in DMEM from 10^{-1} to 10^{-8}. At 72 h after injection, the TCID50 was calculated based on the Reed–Muench method and cytopathic results (Yu et al., 2018).

2.2. Cell viability assay and determination of the antiviral effective concentration of LNFPI

Herein, 10^4 RD cells/well were seeded in 96-well plates. Each well was loaded with DMEM containing different concentrations of LNFPI (25, 50, 100, 200, 400, 800, 1600 and 3200 µg/mL). After 48 h, 10 µL of Cell-Counting Kit-8 (CCK-8) solutions (Beyotime Biotech) were added. After 2–4 h, the absorbance was measured at 450 nm to calculate the cell viability. Crystal violet staining was performed to determine the effectiveness of LNFPI treatment. Briefly, cells were cultured to 80% growth in a 48-well plate, pre-treated with LNFPI (25, 50, 100, 200, 400, 800, and 1600 µg/mL) for 2 h and infected with EV71 having MOI of 1. After changing with fresh 2% DMEM, incubation was continued for 12–16 h. Thereafter, 4% paraformaldehyde was used to fix RD cells at 37 °C for

10 min. After staining with crystal violet for 30 min, the excess crystal violet was washed, and microscopic photographs were taken for recording. Moreover, lactate dehydrogenase (LDH) examination was performed to verify the antiviral effect of LNFPI. The cells were cultured to 70% in 96-well plates and pre-treated with 200 µL of LNFPI (25, 50, 100, 200, 400, 800, and 1600 µg/mL) for 2 h. Thereafter, EV71 with MOI of 1 was added. After 1 h, 20 µL of LDH release reagent was added. For another 1 h, 120 mL of supernatant was taken and mixed with 60 mL of LDH detection working solution for 30 min. The absorbance was measured at 490 nm, and the LDH activity was calculated using sodium pyruvate as a standard curve.

2.3. Time-of-addition experiment

RD cells were seeded into a 96-well plate and were then infected with EV71 having MOI of 1 for 2 h when the cells grew 70%–80%. Thereafter, a fresh medium with 2% FBS was used to continue the cultivation. LNFPI was added at different times (-2, 0, 2, 4, 8, and 12 h). After 24 h, the virus inhibition rate was determined using CCK-8 analysis (Beyotime Biotech).

2.4. Measurements of superoxide dismutase (SOD), malondialdehyde (MDA), ROS and Hoechst 33,258 staining

The SOD activity and MDA level were assessed using a SOD activity detection kit and an MDA assay kit, respectively (Jiancheng, Nanjing, China). Briefly, cells were cultured in 2% DMEM with various concentrations of LNFPI and ribavirin. At 2 h after infection with EV71 having MOI of 1, the medium was replaced with 2% DMEM, and cells were cultured for 12–16 h. When cells appeared distinct morphologically from normal cells, the cells were extracted using Western and IP cell lysate (Beyotime Biotech). The SOD activity and MDA level were determined according to the kit instructions. In addition, ROS generation and nuclear change were assessed using the ROS assay kit (Beyotime Biotech) and Hoechst 33,258 (Solarbio, Beijing, China). Thereafter, 1×10^6 RD cells/well were plated in 6-well plates and treated with LNFPI 2 h before adding the virus with MOI of 1. After 12–16 h, RD cells were incubated with dichloro-dihydro-fluorescein diacetate (DCFH-DA) dilution and Hoechst 33,258 at 37 °C for 20 min and 2 h, respectively. The ROS level was measured under a fluorescence microscope with an excitation wavelength of 488 nm and an emission wavelength of 525 nm.

2.5. Caspase activity

RD cells were initially cultured in a T25 container. The cells were collected by centrifugation at 800 g and 4 °C until each group had at least 2×10^6 cells. Thereafter, 100 µL of caspase lysis buffers were used to extract caspase protein. The supernatant was taken and mixed with detection buffer, incubated at 37 °C for 120 min and then measured at 405 nm. In addition, the protein concentration of cell lysates was measured using a bicinchoninic acid protein concentration determination kit (Beyotime Biotech). The peptide nucleic acid was diluted into different gradients (0, 10, 20, 50, and 100 µM) to make a standard curve.

2.6. Apoptosis and cell cycle detection

For this experiment, 1×10^6 RD cells/well were seeded in 6-well plates and treated with 100, 200, and 400 µg/mL LNFPI and 50 µg/mL ribavirin. After 12 h of viral invasion, cells were collected by centrifugation at 800 rpm/min. Thereafter, 1×10^5 cells were mixed with 500 µL of the binding solution, 5 µL of Annexin V-FITC and 5 µL of propidium iodide (PI) for apoptosis detection, while cells that only stained with PI were used for cell cycle detection. After 10 min of incubation, the FACSCalibur Flow Cytometer (BD Biosciences, CA, USA) was used for apoptosis detection. The number of cells was analysed

using FlowJo 8.8.6 (Tree Star Inc., Ashland, OR, USA).

2.7. C. Elegans culture, synchronisation and administration and examination of cell apoptosis

Wild-type *C. elegans* was obtained from the Sunybiotech (Fujian, China) and was settled on nematode growth media (NGM, containing peptone, NaCl, K_2HPO_4-KH_2PO_4, $MgSO_4$, $CaCl_2$, cholesterol-ethanol, and penicillin–streptomycin) and fed with *E. coli* OP50. *C. elegans* were synchronised by alkaline sodium hypochlorite and grown on NGM plates until the L4 stage. Thereafter, *C. elegans* were transferred to a fresh NGM medium by a picker and divided into three groups as follows: *C. elegans* that received *E. coli* OP50 only and *C. elegans* treated with *E. coli* OP50 containing 100 and 200 µg/mL. *C. elegans* samples were added to fresh NGM plates seeded with fresh *E. coli* OP50 with or without LNFPI in 3 consecutive days.

A total of 70 synchronised *C. elegans* treated with 100-µg/mL and 200-µg/mL LNFPI for 3 days were gathered and incubated with 100 µL of 25-µg/mL acridine orange DNA dye for 1 h. After transferring to fresh NGM medium to recover for 10 min, the *C. elegans* were subjected to 3% agarose containing 20 mM levamisole and observed under the fluorescence microscope with excitation and emission wavelengths of 485 nm and 535 nm.

2.8. Quantitative reverse-transcription polymerase chain reaction (RT-qPCR)

The primers were designed in NCBI (https://www.ncbi.nlm.nih.gov/gene). Primer sequences are listed in Table S1. The total RNA of cells and *C. elegans* was extracted using TRIzol® (CW Biotech, Beijing, China). A cDNA synthesis kit (Takara Bio Inc., Japan) was used to reverse transcribe RNA to cDNA. RT-qPCR was performed in ABI 7300 (Applied Biosystem, CA, USA) using SYBR Premix Ex Taq II kit (Takara Bio Inc.) with the following conditions: denaturation step for 30 s at 95 °C, annealing for 30 s at 60 °C, and extension for 40 s at 72 °C. In this experiment, GADPH was used as internal reference genes, and $2^{-\Delta\Delta CT}$ was used to quantitatively analyse the mRNA of genes.

2.9. Western blot

The total protein of RD cells was extracted using Western and IP cell lysates (Beyotime Biotech) and denatured with sodium dodecyl sulphate at 100 °C for 5 min. Thereafter, 30 µg of protein was added with gel. After transferring to PVDF membrane, the protein was mixed with primary antibodies including cyclin E and CDK2 (Cell Signaling Technology, Danvers, MA, USA). Secondary antibodies labelled with horseradish peroxidase were purchased from Beyotime Biotech. Protein blots were visualised using an enhanced chemiluminescence detection reagent (Beyotime Biotech).

2.10. 16S rRNA gene determination of C. Elegans intestinal flora

Five days after the administration of 100-µg/ml LNFPI, 100*C. elegans* at the L4 stage were collected and resolved in the cell lysis buffer. The DNA was extracted using DNeasy PowerSoil DNA Isolation Kit (Qiagen, Hilden, Germany), and 16S rDNA V4 amplification and PCR were performed. The primers were 5′-GTGCCAGCMGCCGCGGTAA-3′ and 5′-GGACTACHVGGGTWTCTAAT-3′. Amplification was implemented for 32 cycles with the following conditions: initial denaturation at 94 °C for 5 min, denaturation at 94 °C for 30 s annealing at 50 °C for 30 s and extension at 72 °C for 60 s. Bacterial DNAs were monitored by Illumina Miseq PE250 high-throughput sequencing platform. Bioinformatic analysis of sequencing results was processed using Quantitative Insights into Microbial Ecology 1.8.0. Spearman's rho method was used to calculate the correlation between the flora and gene index. RStudio 1.4.1717 and Cytoscape 3.7.0 were used for visual analysis.

2.11. Molecular docking

The 3D model of EV71 capsid protein VP1 was searched through the protein database (https://www.rcsb.org/) and was processed through Schrödinger software. LNFPI was previously synthesised by our group (Zhao et al., 2016). The LNFPI structural formula was Fucα1-2Galβ1-3GlcNAcβ1-3Galβ1-4Glc. The 3D structure of LNFPI was drawn using ChemDraw3D 20.0 and processed by AutoDock. Docking simulations were performed using AutoDock Vina to generate docked results. The results were visualised using PyMOL 2.5.

2.12. Statistics analysis

In all statistical analyses, data were presented as mean $\pm$ SD, and visual fluorescence intensity was calculated by Image-Pro Plus 6.0. Differences between the two groups were assessed using Student's *t*-test. One-way ANOVA of variance was employed to compare the average means of multiple groups. P-value<0.05 and 0.01 was considered statistically to be significant.

3. Results and discussion

3.1. Cytotoxicity and inhibition of LNFPI to EV71

Before investigating the cytotoxicity of EV71, CCK-8 assay was performed to investigate cell survival rate after LNFPI pre-treatment. Under different doses, the highest cytotoxicity was found in the 3200-µg/mL LNFPI group, and no toxic reaction below 1600 µg/mL was noted (Fig. 1a). To determine the effective concentration of LNFPI against EV71, six doses of LNFPI were selected. LNFPI > 400-µg/mL and 50-µg/mL ribavirin treatment effectively guaranteed cell survival rate 12 h after injection with a virus having MOI of 1 (Fig. 1b). Dyed crystal violet exhibited a distinct colour between the normal group and the EV71 group 12 h after injection, and > 400-µg/mL LNFPI could protect RD cells from death (Fig. 1c). The destruction of the cell membrane structure caused by cell apoptosis or necrosis releases enzymes into the culture medium, including stable LDH (Rai et al., 2017). Increasing LDH activity after cell death was observed in the EV71 group, whereas LNFPI protected RD cells from producing LDH (Fig. 1d). To explore the inhibitory stage of LNFPI against EV71 in RD cells, we performed time-of-addition experiment, in which a similar inhibitory stage was observed at 1600 µg/mL LNFPI and 50 µg/mL ribavirin. This indicated that the preventive effect of LNFPI was better than the treatment effect (Fig. 1e). These results presented that pre-treatment of 400-µg/mL LNFPI could effectively protect RD cells.

3.2. LNFPI reduces EV71 invasion by binding with viral capsid VP1 protein

Many studies on vaccines have paid attention to directed therapy targeted capsid VP1 protein since VP1 was considered to be involved in viral invasion (Ch'ng et al., 2011; Wang et al., 2019). Thus, we tested the relative mRNA levels of VP1 in RD cells after 16 h (Fig. 2a). The mRNA levels of VP1 decreased markedly only in the 400-µg/mL LNFPI group. Many studies have demonstrated that natural antivirals had better capability in reducing VP1 expression (Gao et al., 2020). This means that LNFPI might bind with VP1 to prevent EV71 invasion. To further explore the potential binding site of LNFPI to EV71, LNFPI was visualised using 3D imaging software, where red, green and blue represented oxygen, hydrogen, and nitrogen, respectively (Fig. 2b). Thereafter, molecular docking was performed between LNFPI and the X-ray crystal structure of EV71 (Fig. 2c). The lower the affinity value in molecular docking, the more reliable the docking result (Génesis et al., 2017). There were nine conformations of docking analysed using AutoDock, in which the RMSD values of structures *1*, *4*, and *6* with 0, 1.6 and 1.9, respectively, had excellent docking accuracy (Table S2). The *4* conformations showed that
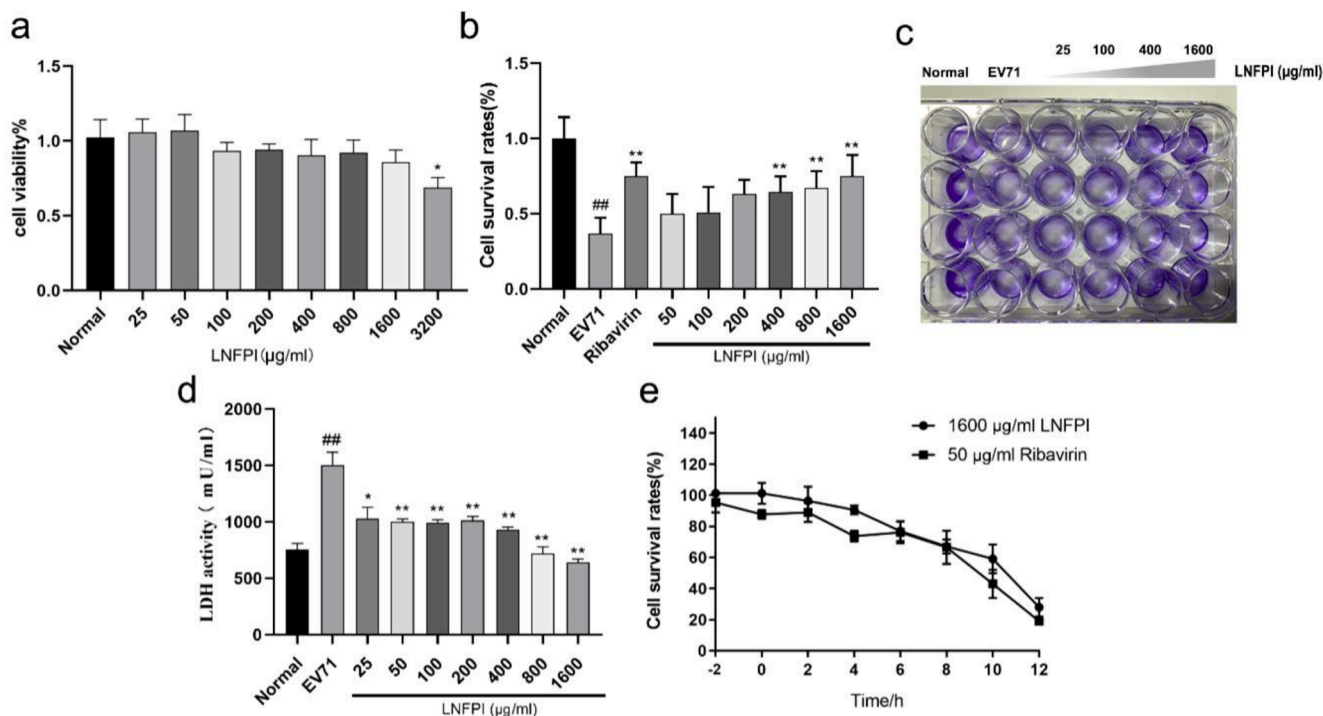
Fig. 1. Cytotoxicity of LNFPI and its inhibition of EV71 in RD cells. (a, b) Cytotoxicity and anti-EV71 effect of LNFPI were measured using a CCK-8 kit. (c) Dyed crystal violet assay was performed in EV71-induced RD cells pre-treated with LNFPI. (d) The bar graph shows the change in lactic dehydrogenase activity in EV71-induced RD cells with and without LNFPI pre-treatment. (e) The time-of-addition experiment revealed the anti-EV71 effect of LNFPI at different times ($*p < 0.05$, $**p < 0.01$ compared with the normal group; $\#p < 0.05$, $\#\#p < 0.01$ compared with the model group).
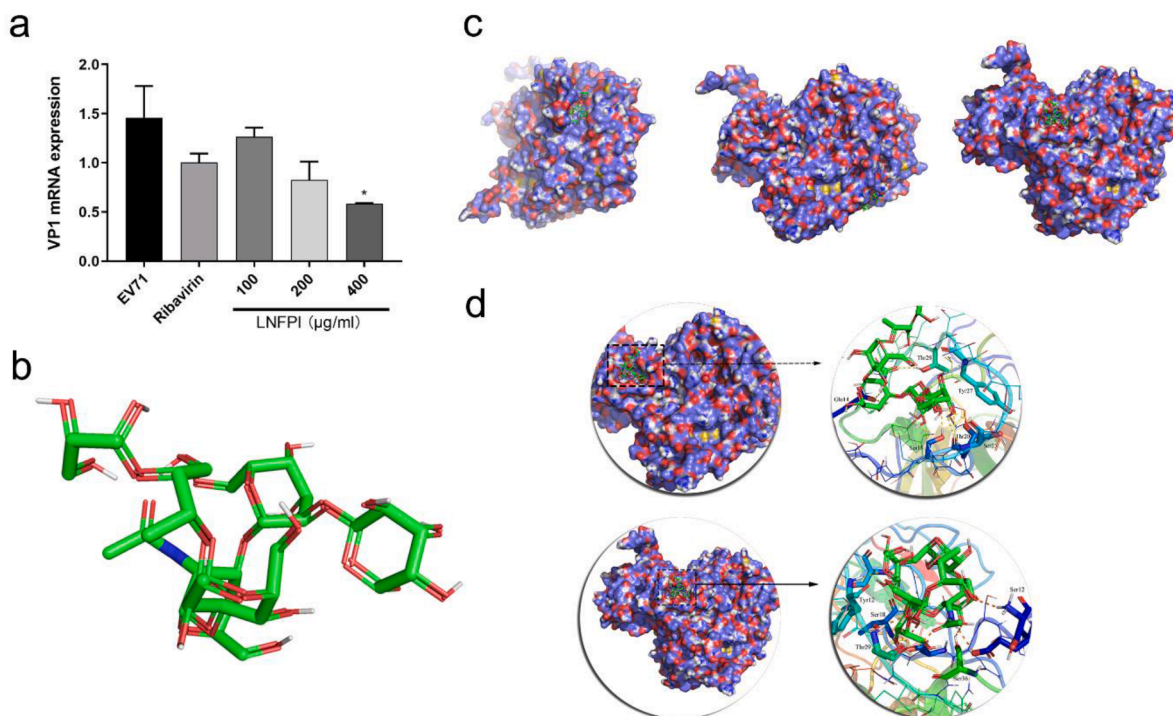

Fig. 2. LNFPI inhibited the attachment of EV71 to RD cells. (a) The total RNA of EV71-induced RD cells pre-treated with LNFPI was extracted for the analysis of VP1 expression using reverse-transcription polymerase chain reaction. (b–d) The molecule structure of LNFPI was visualised via 3D draw. AutoDock exhibited the potential binding sites between EV71 and LNFPI ($*p < 0.05$, $**p < 0.01$ compared with the normal group; $\#p < 0.05$, $\#\#p < 0.01$ compared with the model group).

LNFPI was stabilized by several interactions with the active site residues Glu^{14}, Thr^{29}, Tyr^{27}, Ser^{18}, Thr^{20} and Ser^{23}, while the **6** conformations indicated that the key binding site was composed of Thr^{12}, Ser^{18}, Thr^{29},

Ser^{36} and Ser^{12} (Fig. 2d). Liu et al. found that serine in the epitope of EV71 is a beneficial amino acid for host binding (Liu et al., 2011). However, our results revealed that LNFPI could deter the viral invasion

via monitoring with Ser in EV71, indicating that 400-μg/mL LNFPI could bind to EV71 in several ways, thereby preventing the virus from attaching to the cell, entering the cell and further inhibiting cell apoptosis.

3.3. LNFPI protected RD cells from EV71-induced oxidative stress

After viral invasion, the body experienced oxidative stress, and the cell oxidation balance was disrupted with the increased secretions of protease and several oxidative intermediate products, thereby leading to negative phenomena (Li et al., 2018). RD cells significantly demonstrated a low SOD activity and a high MDA level after viral invasion, while 400 μg/mL LNFPI kept SOD activity at the original level compared with the normal group. LNFPI reduced the MDA level in a dose-dependent manner (Fig. 3a, b). Ribavirin also demonstrated these index improvements. Furthermore, remarkable oxidative stress imbalance is often accompanied by increased ROS levels (Li et al., 2017). DCFH-DA-stained RD cells with EV71 invasion were observed via fluorescence microscope to explore the inhibitory effects of LNFPI on ROS generation (Fig. 3c, d). The ROS level in RD cells infected with EV71 significantly increased. After LNFPI treatment for EV71 invasion for 16 h, the ROS levels in the 400-μg/mL LNFPI group remarkably decreased. Dang et al. also revealed a dramatic change in MDA, SOD and ROS levels, which was consistent with our results (Dang et al., 2017). These results demonstrated that LNFPI could relieve oxidative stress and inhibit damage from EV71, all of which led to cell survival.

3.4. LNFPI protected RD cells from EV71-induced apoptosis

Excessive oxidative stress could lead to cell apoptosis and eliminate useless or damaged cells in the body, thereby maintaining DNA integrity. However, excessive cell apoptosis is detrimental to the body (Lee, 2018). Many viruses can affect apoptosis induction during infection (Tricarico et al., 2017). If apoptosis occurs, crescent-shaped chromatin and dense DNA are found in the nucleus (Bhardwaj and Saraf, 2017). Hoechst 33,258 staining observed under DAPI revealed the presence of

crescent-shaped chromatin in the EV71 group compared with the normal group (Fig. 4a). After introducing 400-μg/mL LNFPI for EV71 invasion for 16 h, the number of crescent-shaped chromatins decreased under $\times$ 100 magnification compared with the EV71 group. In addition, under $\times$ 200 magnification, the DNA in the cell nucleus in the EV71 group became dense. However, the situation was alleviated following LNFPI treatment for 2 h before viral infection. Meanwhile, flow cytometry processing RD cells with PI and Annexin V displayed cell apoptosis as well (Fig. 4b). The proportion of cells in early apoptosis in the EV71 group was 27.7% ± 2.13%, while the rate of cells exposed to 400-μg/mL LNFPI was 10.9% ± 1.26% (Table S3). Cells that stained positive with PI and Annexin V were regarded to be in the late stage of apoptosis. The late apoptosis rate in the EV71 group was 46.4% ± 1.10%; however, the number of RD cells treated with LNFPI decreased at 29.5% ± 1.23%. Ribavirin also showed results comparable with LNFPI. A previous study proved that the use of fructose-enrich substances decreased the apoptosis rate, which confirmed the reliability of our conclusions (Iba et al., 2018; Su et al., 2020). The caspase family was a key regulatory protein in apoptosis and caused the hydrolysis of many proteins (Sandra et al., 2004). To further confirm the effect of LNFPI on EV71-induced apoptosis, the activities of caspase-3, caspase-8 and caspase-9 were measured (Fig. 4c). Quantitative analysis indicated that 400-μg/mL LNFPI significantly inhibited the activity of caspase-3, caspase-8 and caspase-9. Similarly, the mRNA expressions of caspase-3, caspase-8 and caspase-9 were decreased in EV71-infected RD cells after LNFPI treatment (Fig. 4d). The apoptotic pathways were classified into the endogenous mitochondrial pathway and the exogenous death receptor pathway, which complemented each other to induce the activation of caspase-3 and promote apoptosis (Zhao et al., 2017). In the endogenous pathway, the initiation of caspase-3 resulted from the activation of pre-caspase-9 while caspase-8 was activated by the cascade of extracellular death signals to further activate caspase-3 in the exogenous pathway (Brentnall et al., 2013). To further analyse the cause of caspase-3, caspase-8 and caspase-9 difference, the two main apoptosis-related pathways were detected (Fig. 4e). After the invasion, the mRNA expression of poly(ADP-ribose)polymerase (PAPR) and B-cell
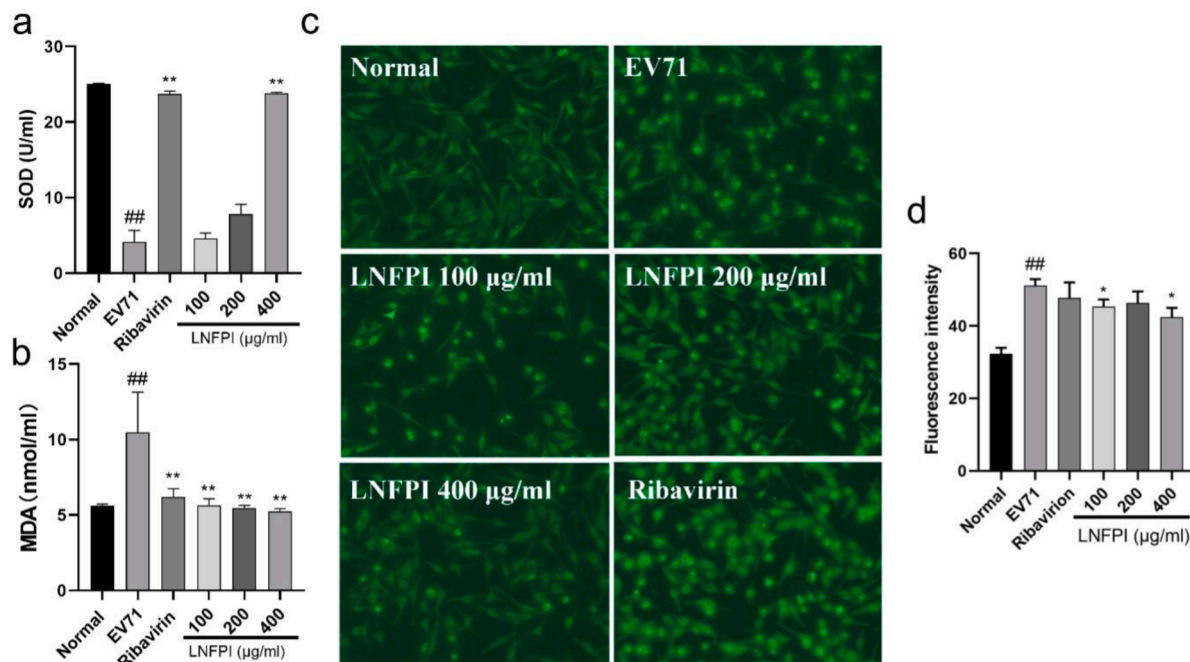

Fig. 3. LNFPI reduced EV71-induced oxidative stress in RD cells. (a, b) The SOD activity and MDA level in EV71-induced RD cells that could affect stress reaction were measured to explore the inhibition of oxidative stress by LNFPI. (c, d) The level of ROS in EV71-induced RD cells was evaluated using DCFH-DA and observed under the fluorescence microscope after LNFPI pre-treatment (*$p < 0.05$, **$p < 0.01$ compared with the normal group; #$p < 0.05$, ##$p < 0.01$ compared with the model group).
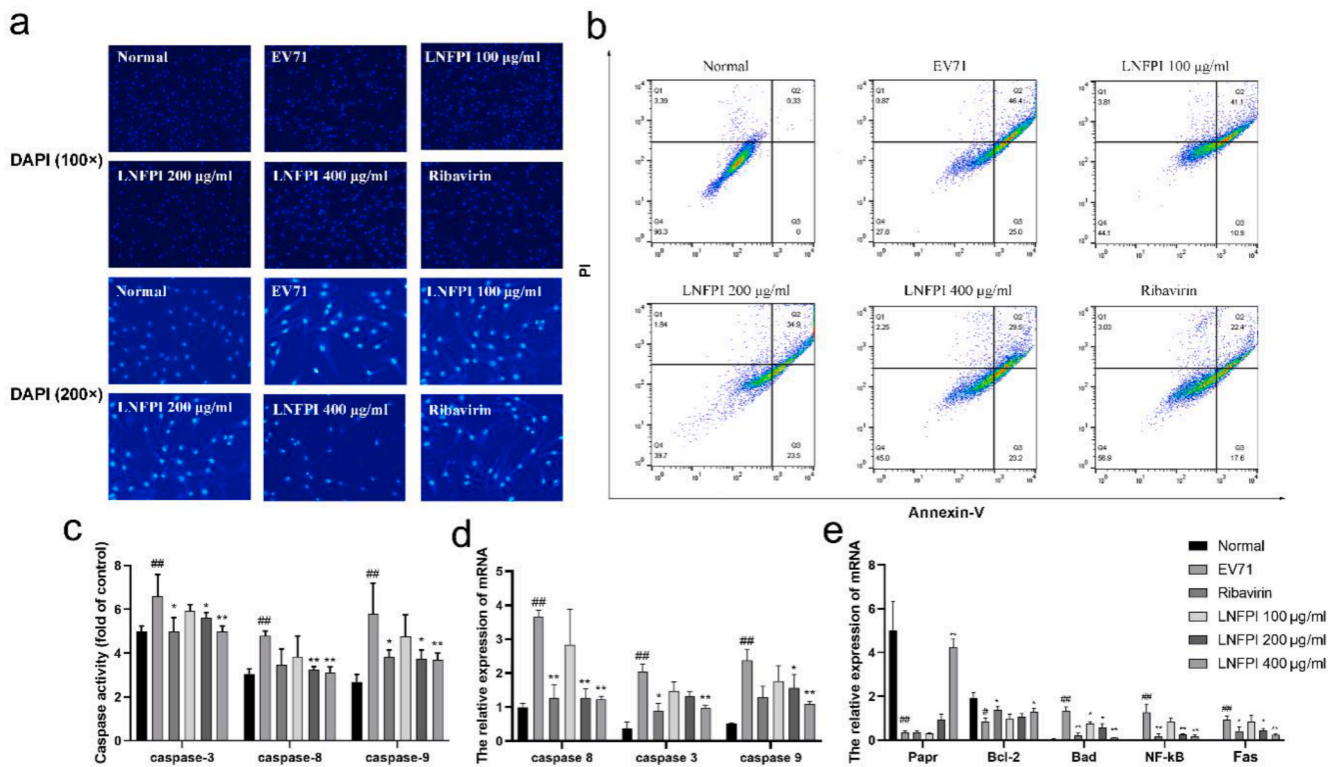
Fig. 4. LNFPI mitigated EV71-associated cell apoptosis in mitochondria-dependent and death-receptor manner. (a) The Hoechst 33,258 assay was performed in EV71-induced RD cells with or without LNFPI pre-treatment and observed using fluorescence microscopy with × 100 and × 200 magnifications. (b) LNFPI affected apoptosis rates of RD cells subjected to PI and Annexin V staining after EV71 invasion using flow cytometry. (c) The caspase activity with and without LNFPI pre-treatment was examined. (d, e) The mRNA expressions of apoptosis-associated genes were calculated and displayed in bar graphs (*$p < 0.05$, **$p < 0.01$ compared with the normal group; #$p < 0.05$, ##$p < 0.01$ compared with the model group).
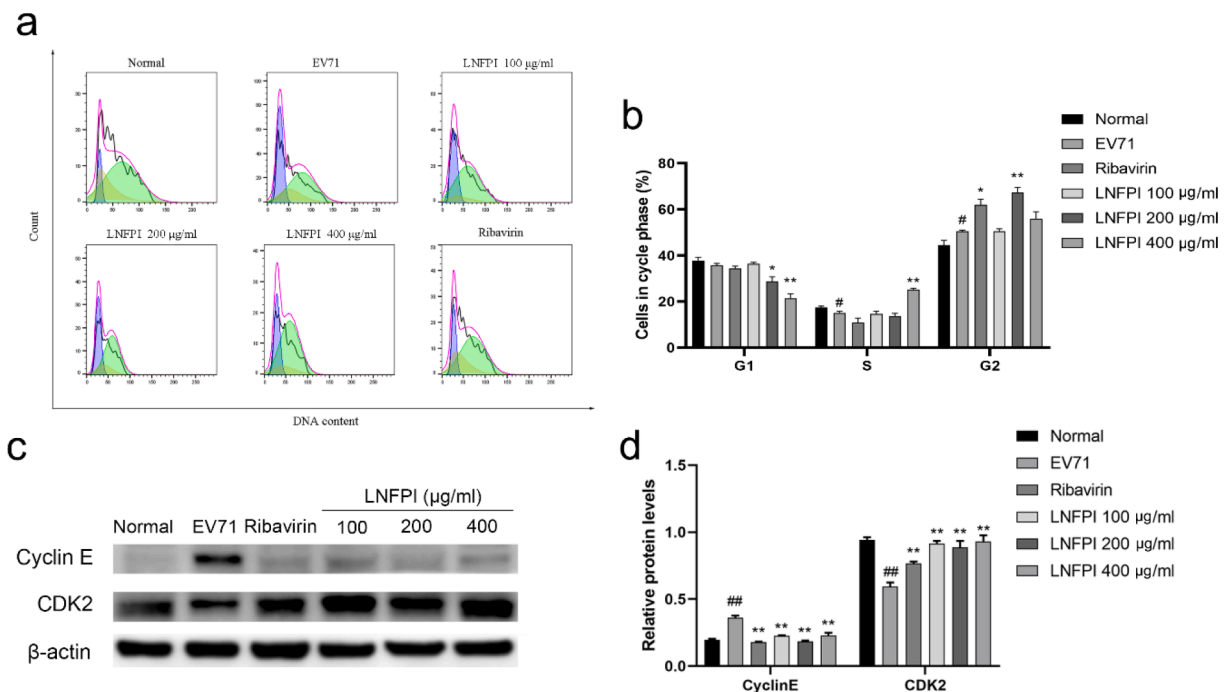

Fig. 5. LNFPI leads to the recovery of EV71-induced S phase arrest in RD cells. (a, b) Flow cytometry was used to analyse EV71-induced RD cells stained with PI to investigate the influence of LNFPI on the cell cycle. (c, d) Western blot assay was employed to explore the effect of LNFPI on cyclin-related protein after EV71 invasion. The bar graph shows quantification of the cyclin E/β-actin and CDK2/β-actin ratios (*$p < 0.05$, **$p < 0.01$ compared with the normal group; #$p < 0.05$, ##$p < 0.01$ compared with the model group).

lymphoma 2 (Bcl-2) remarkably decreased, and the mRNA expression of Bcl-2-associated agonist of cell death (Bad), nuclear factor kappa B (NF-kB) and Fas significantly increased. When Fas was activated and the conformation of Fasl changed, caspase-8 cut the Bad that is located in the mitochondrial membrane, at which cytochrome *C* activated caspase-9 and caspase-3 thereby promoting apoptosis (Sánchez-Bretaño et al., 2017). Meanwhile, NF-kB and Bcl-2, regarded as cell protection factors, could directly inhibit the activation of caspase-8, and PAPR could repair the damaged DNA to inhibit apoptosis (Gobeil et al., 2001; Xie et al., 2017). LNFPI recovered the decreased mRNA expression of PAPR, NF-kB and Bcl-2 and properly regulated Bad and Fas into their normal levels. These results presented that LNFPI could inhibit Fas and Bad expression, thus inhibiting the EV71-induced apoptosis in death-receptor and mitochondria-dependent manner.

3.5. LNFPI protected RD cells from EV71-induced cell cycle arrest

To understand the potential mechanism that led to apoptosis, the hypothesis that cell cycle arrest initiated apoptosis was proposed. When the cell cycle was blocked, cells would trigger cell apoptosis to eliminate cells with abnormal DNA replication, thereby maintaining DNA stability (Liu et al., 2018; Song et al., 2018). DNA content demonstrated that arrest occurred in the S phase in RD cells after EV71 invasion; however,

LNFPI promoted the transition of the G1 phase to the S phase and the DNA contents were even higher than that in the normal group (Fig. 5a, b). CDK2 is a cyclin-dependent kinase that can interact with cyclin to promote the cell cycle (Ning et al., 2017), and decreased cyclin E is responsible for S phase transformation (Yu et al., 2015). To further explore the mechanism of LNFPI on the cell cycle after viral invasion, cyclin E and CDK2 were involved. Western blotting analysis indicated that cyclin E expression was significantly increased in RD cells after LNFPI treatment compared with the EV71 group (Fig. 5c, d). Meanwhile, CDK2 expression reported an increasing trend in the LNFPI group compared with the EV71 group. Zhong et al. found decreased cyclin E and increased CDK2 levels after EV71 invasion, which was similar to our results (Yu et al., 2015). These results demonstrated that EV71 perturbed cell cycle progression and LNFPI maintained the cell cycle balance and facilitated the transition of the S phase, thereby inhibiting cell apoptosis.

3.6. LNFPI inhibited cell apoptosis in C. elegans

C. elegans is considered the classical model for apoptosis (Sherrard et al., 2017). *C. elegans* was used to further verify the anti-apoptotic effect of LNFPI. After 3 days of LNFPI treatment, some regions had lower levels of acridine orange staining that is related to apoptosis in
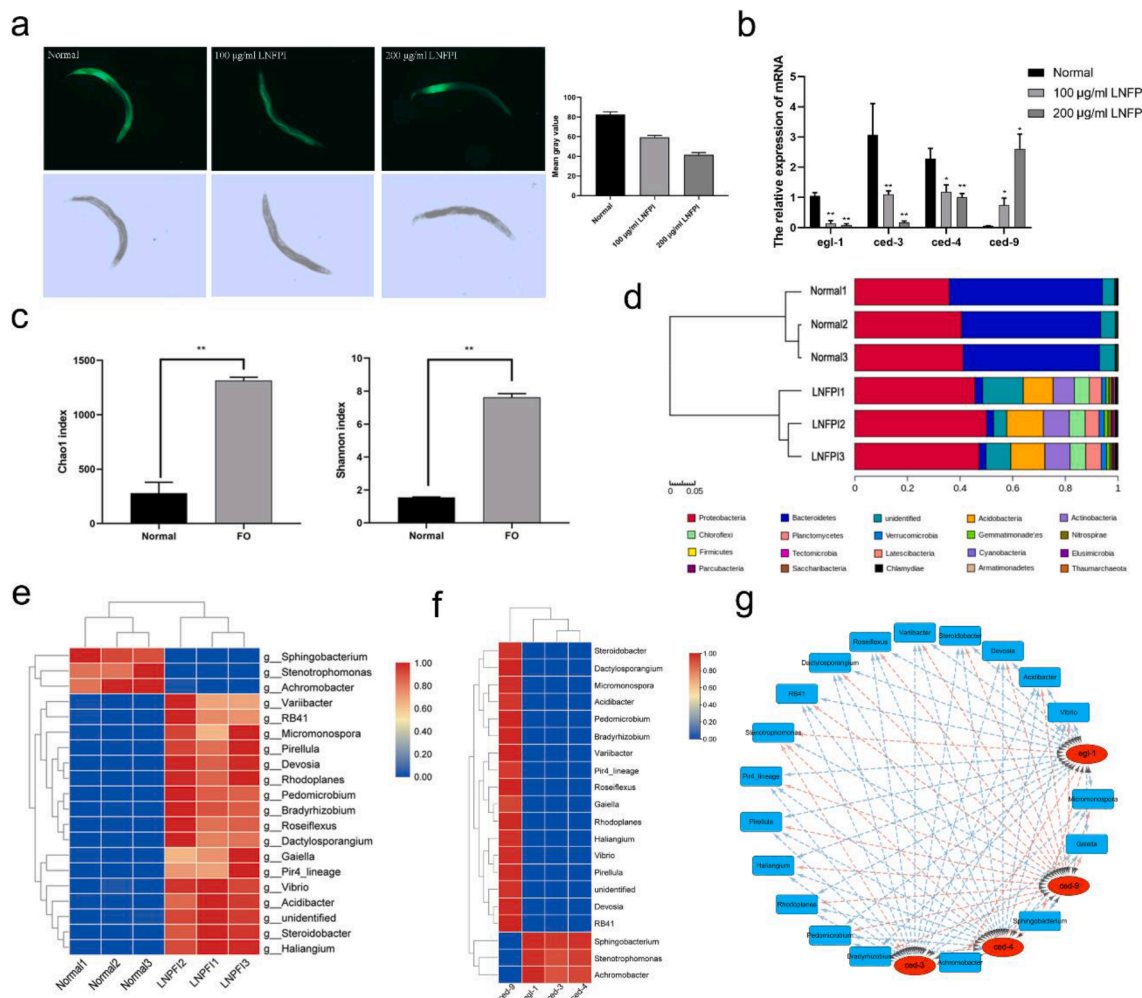

Fig. 6. Anti-apoptotic effect of LNFPI treatment on *C. elegans* and its intestinal flora. (a) Acridine orange staining assay showed the anti-apoptotic effect of LNFPI, and bar graphs indicated the relative mean fluorescence. (b) Bar graphs showed the relative mRNA expression of apoptotic genes. (c) The change in Chao1 and Shannon indices of intestinal flora after LNFPI treatment. (d) Difference in bacteria at the phylum level between *C. elegans* with or without LNFPI pre-treatment. (e) Top abundant bacteria at the genus level. (f, g) Spearman correlation analysis of apoptosis-related genes and their intestinal flora. Red means positive and blue means negative (*$p < 0.05$, **$p < 0.01$ compared with the normal group; #$p < 0.05$, ##$p < 0.01$ compared with the model group).

nematodes compared with the normal group (Fig. 6a). In addition, the quantitative analysis revealed significant changes either in the 100 µg/mL or 200 µg/mL LNFPI group compared with the normal group. Three pro-apoptotic genes were found in *C. elegans*, including *Egl-1*, *Ced-3* and *Ced-4*. These genes promoted the apoptosis of nematode germ cells. However, *Ced-9*, an apoptosis regulator, can protect apoptosis caused by nematodes during growth and development (Guardia et al., 2016). To investigate the anti-apoptotic effect of LNFPI, *Egl-1*, *Ced-3*, *Ced-4* and *Ced-9* were examined via RT-qPCR (Fig. 6b). Moreover, 100-µg/mL and 200-µg/mL LNFPI significantly decreased the levels of *Egl-1*, *Ced-3* and *Ced-4* compared with the normal group. *Ced-9* exhibited an uptrend after LNFPI treatment. Therefore, LNFPI could reduce the occurrence of *C. elegans* apoptosis by inhibiting the apoptosis pathway.

3.7. LNFPI regulated apoptosis-related gut microbiota

In addition to inhibiting pathogen invasion, LNFPI could regulate intestinal microbiota thereby affecting immune system development (Walsh et al., 2020). Therefore, the potential anti-apoptotic effect of LNFPI via the gut microbiota in *C. elegans* was investigated. After data processing, a total of 52,370 samples were read. The Chao1 and Shannon indices reflected the α-diversity of the intestinal flora. The Chao1 index indicated the difference in the abundance of species. The Shannon index was based on the abundance of the flora, which reflected the uniformity of the species and some rare operational taxonomic units (OTUs) (Seishima et al., 2019). After the *C. elegans* were treated with LNFPI, the Chao1 and Shannon indices were higher in the LNFPI group than in the normal group ($p < 0.01$) (Fig. 6c). These results showed that after LNFPI treatment, the species diversity of the gut microbiota was changed largely compared with that of the normal group. The principal component analysis (PCA) and principal coordinate analysis (PCoA) of the weighted UniFrac distance based on OTUs showed distinct changes in the composition of the gut microbiota between the normal group and the LNFPI group (Fig. S1).

The stacked chart presented that at the phylum level, the intestinal flora of *C. elegans* is mainly composed of *Proteobacteria*, *Bacteroides* and some undefined bacteria (Fig. 6d). After LNFPI treatment, the composition of the gut microbiota in nematodes indicated significant changes in *C. elegans*. Interestingly, the proportion of *Proteobacteria* remarkably increased, whereas that of *Bacteroides* decreased significantly after LNFPI treatment. LNFPI nourishes other microbiota and thereby causes a significant decrease in the proportion of *Bacteroides*. A similar phenomenon has been reported in breastfed and non-breastfed infants (Marcobal et al., 2012; Smith-Brown et al., 2016). Meanwhile, the proportions of *Acidobacteria*, *Actinomycetes*, *Chloroflexi*, *Planktomycetes*, *Verrucomicrobia*, *Gemmatimonadetes,* and *Nitrospirae* in the LNFPI group increased significantly compared with the normal group. The proportions of the intestinal microbiota at the genus level in normal nematodes were also very distinct from that in LNFPI-treated nematodes (Fig. 6e). The intestinal microbiota that ranked top 20 was identified to explore potential biomarkers of intestinal flora. LNFPI significantly reduced the abundance of *Sphingobacterium*, *Stenotrophomonas* and *Achromobacter*. On the contrary, with the exclusion of undefined bacteria, LNFPI also significantly increased the abundance of *Micromonospora*, *Vibrio*, *Acidibacter*, *Gaiella*, *Devosia*, *Steroidobacter*, *Variibacter*, *D*actylosporangium, *RB41*, *Pir4_lineage*, *Pirellula*, *Haliangium*, *Roseiflexus*, *Pedomicrobium,* and *Bradyrhizobium*. These changes demonstrated that LNFPI had an excellent effect on improving the composition of the intestinal flora. However, the further specific relationship between intestinal microbiota and apoptosis after LNFPI treatment was unknown (Fig. 6f, g). Significant changes in the gut microbiota were again examined, and apoptosis-related genes were selected. Correlation analysis based on the Pearson correlation coefficient was employed. The correlation analysis showed that *Sphingosine*, *Stenotrophomonas* and *Achromobacteria* in *C. elegans* were positively correlated with the nematode apoptosis genes *Egl-1*, *Ced-3* and *Ced-4* and

negatively correlated with *Ced-9*. This indicated that the increase in the abundance of these three bacteria could promote nematode cell apoptosis. However, the increase in the abundance of *Micromonospora*, *Vibrio*, *Acidibacter*, *Gaiella*, *Devosia*, *Steroidobacter*, *Variibacter*, *Roseiflexus*, *Dactylosporangium*, *RB41*, *Pir4_lineage*, *Pirellula*, *Haliangium*, *Pedomicrobium,* and *Bradyrhizobium* were highly positive with *Ced-9* and negative with *Egl-1*, *Ced-3* and *Ced-4*. Possibly, LNFPI increased the apoptosis rate in *C. elegans* by regulating intestinal microbiota to promote or inhibit gene transcription or translation. *Sphingosine* induced apoptosis and caused inflammation of the mammary glands (Sivaramakrishna et al., 2019). *Stenotrophomonas* also induced inflammation, leading to bodily dysfunctions (Kim et al., 2016). Similarly, *Achromobacteria* caused a sharp worsening in lung inflammation of patients with cystic fibrosis (Hansen et al., 2010). These reports indicated that all three bacteria can trigger apoptosis through inflammation. In addition to anti-apoptosis of intestinal microbiota, studies have reported that the microbiota had significant anti-inflammatory and antibacterial effects. *Micromonospora* had strong antibacterial activity and inhibited the invasion of pathogenic agents (Pérez-Bonilla et al., 2018). *Dactylosporangium* produced *trans*-4-hydroxy-proline through genetic engineering technology to inhibit the development of inflammation (Zhang et al., 2019). *Bradyrhizobium* had good immunological activity and inhibited the expression of inflammatory receptor TLR4 both *in vivo* and *in vitro* (Lembo-Fazio et al., 1888). Together, bacteria degrade many substances such as alkaloids and polysaccharides to increase the lifespan of nematodes in *C. elegans* (Zhang et al., 2017; Chen et al., 2020). During degradation, the microbiota release metabolites or effector molecules to activate apoptotic receptors (Lebeer et al., 2018). LNFPI decrease apoptosis rate because of the significant change in the microbiota structure. Therefore, intestinal microbiota would play an important role in anti-apoptosis and inhibition of nematode cell apoptosis.

4. Conclusion

In this study, we investigated the anti-EV71 and anti-apoptotic effects of LNFPI in EV71-infected RD cells. The results showed that 400-µg/mL LNFPI effectively inhibited capsid protein VP1 and reduced damage caused by EV71 to cells. Molecular docking-predicted LNFPI was likely to combine with EV71, however, the specific mechanism requires further investigation. Furthermore, LNFPI promoted CDK2 expression and reduced the level of cyclin E to recover EV71-induced S phase arrest for inhibiting apoptosis. LNFPI reduced the apoptosis rate in *C. elegans* possibly through increased relative abundances of beneficial anti-inflammatory bacteria and decreased apoptosis-promoting and inflammation-associated bacteria. These results demonstrated that LNFPI interacted with EV71 to reduce EV71 attachment and apoptosis rate and might be a promising supplement with antiviral properties for the prevention of viral diseases.

Declaration of Competing Interest

The authors declare that they have no known competing financial interests or personal relationships that could have appeared to influence the work reported in this paper.

Appendix A. Supplementary data

Supplementary data to this article can be found online at https://doi.org/10.1016/j.fochx.2022.100244.

References

Bhardwaj, J. K., & Saraf, P. (2017). N-acetyl cysteine-mediated effective attenuation of methoxychlor-induced granulosa cell apoptosis by counteracting reactive oxygen species generation in caprine ovary. *Environmental Toxicology, 32*(1), 156–166.

Bode, L., & Jantscher, K. E. (2012). Structure-function relationships of human milk oligosaccharides. *Adv Nutr, 3*(3), 383S–391S.

Brentnall, M., Rodriguez-Menocal, L., De Guevara, R. L., Cepero, E., & Boise, L. H. (2013). Caspase-9, caspase-3 and caspase-7 have distinct roles during intrinsic apoptosis. *BMC Cell Biol., 14*(1), 32.

Ch'ng, W.-C., Stanbridge, E. J., Ong, K.-C., Wong, K.-T., Yusoff, K., & Shafee, N. (2011). Partial protection against enterovirus 71 (EV71) infection in a mouse model immunized with recombinant Newcastle disease virus capsids displaying the EV71 VP1 fragment. *Journal of Medical Virology, 83*(10), 1783–1791.

Dang, D., Zhang, C., Zhang, R., Wu, W., Chen, S., Ren, J., … Duan, G. (2017). Involvement of inducible nitric oxide synthase and mitochondrial dysfunction in the pathogenesis of enterovirus 71 infection. *Oncotarget., 8*(46), 81014–81026.

Feng, Q., Chen, W. D., & Wang, Y. D. (2018). Gut microbiota: An integral moderator in health and disease. *Frontiers in Microbiology, 9*, 151.

Gao, X., Wu, D., Wen, Y., Gao, L., Liu, D., Zhong, R., … Zhao, C. (2020). Antiviral effects of human milk oligosaccharides: A review. *International Dairy Journal, 110*, 104784. https://doi.org/10.1016/j.idairyj.2020.104784

Gobeil, S., Boucher, C. C., Nadeau, D., & Poirier, G. G. (2001). Characterization of the necrotic cleavage of poly (ADP-ribose) polymerase (PARP-1): Implication of lysosomal proteases. *Cell Death and Differentiation, 8*(6), 588–594.

Guardia, Y., Gilliat, A. F., Hellberg, J., Rennert, P., Cabreiro, F., & Gems, D. (2016). Run-on of germline apoptosis promotes gonad senescence in *C. elegans. Oncotarget, 7*(26), 39082–39096.

Hansen, C. R., Pressler, T., Nielsen, K. G., Jensen, P.Ø., Bjarnsholt, T., & Høiby, N. (2010). Inflammation in *Achromobacter xylosoxidans* infected cystic fibrosis patients. *Journal of Cystic Fibrosis, 9*(1), 51–58.

Hu, Y., Zeng, G., Chu, K., Zhang, J., Han, W., Zhang, Y., … Zhu, F. (2018). Five-year immunity persistence following immunization with inactivated enterovirus 71 type (EV71) vaccine in healthy children: A further observation. *Hum Vacc Immunother, 14*(6), 1517–1523.

Iba, T., Hirota, T., Sato, K., & Nagaoka, I. (2018). Protective effect of a newly developed fucose-deficient recombinant antithrombin against histone-induced endothelial damage. *International Journal of Hematology, 107*(5), 528–534.

Kim, Y. J., Jeon, H., Na, S. H., Kwon, H. I., Selasi, G. N., Nicholas, A., … Carbonetti, N. (2016). *Stenotrophomonas maltophilia* outer membrane vesicles elicit a potent inflammatory response *in vitro* and *in vivo. Pathog Dis, 74*(8), ftw104. https://doi.org/10.1093/femspd/ftw104

Koromyslova, A., Tripathi, S., Morozov, V., Schroten, H., & Hansman, G. S. (2017). Human norovirus inhibition by a human milk oligosaccharide. *Virology, 508*, 81–89.

Lars, B., & Evelyn, J. K. (2012). Structure-function relationships of human milk oligosaccharides. *Adv Nutr, 1*(3), 383–391.

Lee, C. (2018). Therapeutic modulation of virus-induced oxidative stress via the Nrf2-dependent antioxidative pathway. *Oxid Med Cell Longev, 2018*, 1–26.

Lembo-Fazio, L., Billod, J.-M., Di Lorenzo, F., Paciello, I., Pallach, M., Vaz-Francisco, S., … Silipo, A. (1888). *Bradyrhizobium* Lipid A: Immunological properties and molecular basis of its binding to the myeloid differentiation protein-2/toll-like receptor 4 complex. *Frontiers in Immunology, 9*. https://doi.org/10.3389/fimmu.2018.0188810.3389/fimmu.2018.01888.s001

Li, M., Monaco, M. H., Wang, M., Comstock, S. S., Kuhlenschmidt, T. B., Fahey Jr, G. C., … Donovan, S. M. (2014). Human milk oligosaccharides shorten rotavirus-induced diarrhea and modulate piglet mucosal immunity and colonic microbiota. *ISME Journal, 8*(8), 1609–1620.

Li, Y., Lin, Z., Xu, T., Wang, C., Zhao, M., Xiao, M., … Zhu, B. (2017). Delivery of VP1 siRNA to inhibit the EV71 virus using functionalized silver nanoparticles through ROS-mediated signaling pathways. *RSC Advances, 7*(3), 1453–1463.

Lin, Z., Li, Y., Gong, G., Xia, Y., Wang, C., Chen, Y., … Zhu, B. (2018). Restriction of H1N1 influenza virus infection by selenium nanoparticles loaded with ribavirin via resisting caspase-3 apoptotic pathway. *International Journal of Nanomedicine, 13*, 5787–5797.

Liu, J., Li, Q., Li, X., Qiu, Z., Li, A., Liang, W., … Li, H. (2018). Zika virus envelope protein induces G2/M cell cycle arrest and apoptosis via an intrinsic cell death signaling pathway in neuroendocrine PC12 cells. *International Journal of Biological Sciences, 14*(9), 1099–1108.

Liu, Y.-S., Zhou, J.-H., Chen, H.-T., Ma, L.-n., Pejsak, Z., Ding, Y.-Z., & Zhang, J. (2011). The characteristics of the synonymous codon usage in enterovirus 71 virus and the effects of host on the virus in codon usage pattern. *Infection, Genetics and Evolution, 11*(5), 1168–1173.

Morozov, V., Hansman, G., Hanisch, F.-G., Schroten, H., & Kunz, C. (2018). Human milk oligosaccharides as promising antivirals. *Molecular Nutrition & Food Research, 62*(6), 1700679. https://doi.org/10.1002/mnfr.201700679

Ning, P., Hu, C., Li, X., Zhou, Y., Hu, A., Zhang, Y.a., … Zhang, Y. (2017). Classical swine fever virus Shimen infection increases p53 signaling to promote cell cycle arrest in porcine alveolar macrophages. *Oncotarget, 8*(34), 55938–55949.

Pérez-Bonilla, M., Oves-Costales, D., de la Cruz, M., Kokkini, M., Martín, J., Vicente, F., … Reyes, F. (2018). *Phocoenamicins* B and C, new antibacterial spirotetronates isolated from a marine *Micromonospora sp. Marine Drugs, 16*(3), 95. https://doi.org/10.3390/md16030095

Plaza-Díaz, J., Fontana, L., & Gil, A. (2018). Human milk oligosaccharides and immune system development. *Nutrients, 10*(8), 1038.

Rai, G., Brimacombe, K. R., Mott, B. T., Urban, D. J., Hu, X., Yang, S.-M., … Maloney, D. J. (2017). Discovery and optimization of potent, cell-active pyrazole-based inhibitors of lactate dehydrogenase (LDH). *Journal of Medicinal Chemistry, 60*(22), 9184–9204.

Salem, J. B., Nkambeu, B., Arvanitis, D. N., & Beaudry, F. (2018). Deciphering the role of EGL-3 for neuropeptides processing in *Caenorhabditis elegans* using high-resolution quadrupole-orbitrap mass spectrometry. *Neurochemical Research, 43*(11), 2121–2131.

Sánchez-Bretaño, A., Baba, K., Janjua, U., Piano, I., Gargini, C., & Tosini, G. (2017). Melatonin partially protects 661W cells from H2O2-induced death by inhibiting Fas/FasL-caspase-3. *Molecular Vision, 23*, 844–852.

Sandra, F., Degli Esposti, M., Ndebele, K., Gona, P., Knight, D., Rosenquist, M., & Khosravi-Far, R. (2005). Death receptors and intracellular membrane lipids: A view from the mitochondria. *Cancer Research, 65*(18), 8286–8297.

Seishima, J., Iida, N., Kitamura, K., Yutani, M., Wang, Z., Seki, A., … Kaneko, S. (2019). Gut-derived *enterococcus faecium* from ulcerative colitis patients promotes colitis in a genetically susceptible mouse host. *Genome Biology, 20*(1). https://doi.org/10.1186/s13059-019-1879-9

Sherrard, R., Luehr, S., Holzkamp, H., McJunkin, K., Memar, N., & Conradt, B. (2017). miRNAs cooperate in apoptosis regulation during *C. elegans* development. *Genes & Development, 31*(2), 209–222.

Sivaramakrishna, D., Prasad, M. D., & Swamy, M. J. (2019). A homologous series of apoptosis-inducing N–acylserinols: Thermotropic phase behavior, interaction with cholesterol and characterization of cationic N–myristoylserinol-cholesterol-CTAB niosomes. *BBA-Biomembranes, 1861*(2), 504–513.

Song, F., Yu, X., Zhong, T., Wang, Z., Meng, X., Li, Z., … Yu, J. (2018). Caspase-3 inhibition attenuates the cytopathic effects of EV71 infection. *Frontiers in Microbiology, 9*. https://doi.org/10.3389/fmicb.2018.0081710.3389/fmicb.2018.00817.s002

Su, W., Wang, L., Fu, X., Ni, L., Duan, D., Xu, J., & Gao, X. (2020). Protective effect of a fucose-rich fucoidan isolated from *Saccharina japonica* against ultraviolet B-induced photodamage in vitro in human keratinocytes and in vivo in zebrafish. *Marine Drugs, 18*(6), 316.

Tricarico, P. M., Caracciolo, I., Crovella, S., & D'Agaro, P. (2017). Zika virus induces inflammasome activation in the glial cell line U87-MG. *Biochemical and Biophysical Research Communications, 492*(4), 597–602.

Tung, W.-H., Hsieh, H.-L., Lee, I.-T., & Yang, C.-M. (2011). Enterovirus 71 induces integrin β1/EGFR-Rac1-dependent oxidative stress in SK-N-SH cells: Role of HO-1/CO in viral replication. *Journal of Cellular Physiology, 226*(12), 3316–3329.

Walsh, C., Lane, J. A., van Sinderen, D., & Hickey, R. M. (2020). Human milk oligosaccharides: Shaping the infant gut microbiota and supporting health. *Journal of Functional Foods, 72*, 104074. https://doi.org/10.1016/j.jff.2020.104074

Wang, N., Yang, X., Sun, J., Sun, Z., Ma, Q., Wang, Z., … Xu, J. (2019). Neutrophil extracellular traps induced by VP1 contribute to pulmonary edema during EV71 infection. *Cell Death Discov, 5*(1). https://doi.org/10.1038/s41420-019-0193-3

Wang, R. Y. L., Weng, K. F., Huang, Y. C., & Chen, C. J. (2016). Elevated expression of circulating miR876-5p is a specific response to severe EV71 infections. *Scientific Reports, 6*(1), 1–10.

Wang, W., Xiao, F., Wan, P., Pan, P., Zhang, Y., Liu, F., … Luo, G. G. (2017). EV71 3D protein binds with NLRP3 and enhances the assembly of inflammasome complex. *PLoS Pathogens, 13*(1).

Xie, Z., Xiao, Z., & Wang, F. (2017). Hepatitis C Virus nonstructural 5A protein (HCV-NS5A) inhibits hepatocyte apoptosis through the NF-κb/miR-503/bcl-2 pathway. *Molecules and Cells, 40*(3), 202–210.

Yu, J., Zhang, L., Ren, P., Zhong, T., Li, Z., Wang, Z., … Yu, X.-F. (2015). Enterovirus 71 mediates cell cycle arrest in S phase through non-structural protein 3D. *Cell Cycle, 14*(3), 425–436.

Yu, P.-C., Tao, X.-Y., Wang, L.-H., Tang, Q., Fan, L.-Y., Zhang, S.-X., … Zhu, W.-Y. (2018). Establishment of a Chinese street rabies virus library and its application for detecting neutralizing activity. *Infectious Diseases of Poverty, 7*(1). https://doi.org/10.1186/s40249-018-0500-x

Zhang, G., Zhou, F., Gu, B., Ding, C., Feng, D., Xie, F., … Yao, K. (2012). In vitro and in vivo evaluation of ribavirin and pleconaril antiviral activity against enterovirus 71 infection. *Archives of Virology, 157*(4), 669–679.

Zhang, Y.u., Zhang, Y., Shang, X., Wang, B.o., Hu, Q., Liu, S., & Wen, T. (2019). Reconstruction of tricarboxylic acid cycle in *Corynebacterium glutamicum* with a genome-scale metabolic network model for trans-4-hydroxyproline production. *Biotechnology and Bioengineering, 116*(1), 99–109.

Zhao, C., Wu, Y., Yu, H., Shah, I. M., Li, Y., Zeng, J., … Chen, X. (2016). One-pot multienzyme (OPME) synthesis of human blood group H antigens and a human milk oligosaccharide (HMOS) with highly active *Thermosynechococcus* elongatusa1-2fucosyltransferase. *Chemical Communications, 52*(20), 3899–3902.

Zhao, H., He, Y., Li, S., Sun, X., Wang, Y.u., Shao, Y., … Xing, M. (2017). Subchronic arsenism-induced oxidative stress and inflammation contribute to apoptosis through mitochondrial and death receptor dependent pathways in chicken immune organs. *Oncotarget, 8*(25), 40327–40344.